Energy & Environmental Science

ROYAL SOCIETY OF CHEMISTRY

PAPER

View Article Online
View Journal | View Issue

Cite this: *Energy Environ. Sci.*, 2022, **15**, 714

Understanding and suppressing non-radiative losses in methylammonium-free wide-bandgap perovskite solar cells†

Robert D. J. Oliver, ‡[a] Pietro Caprioglio, ‡*[a] Francisco Peña-Camargo, [b] Leonardo R. V. Buizza,[a] Fengshuo Zu,[cd] Alexandra J. Ramadan, [a] Silvia G. Motti,[a] Suhas Mahesh,[a] Melissa M. McCarthy, [a] Jonathan H. Warby,[b] Yen-Hung Lin, [a] Norbert Koch, [cd] Steve Albrecht,[e] Laura M. Herz,[af] Michael B. Johnston, [a] Dieter Neher, [b] Martin Stolterfoht [b] and Henry J. Snaith *[a]

With power conversion efficiencies of perovskite-on-silicon and all-perovskite tandem solar cells increasing at rapid pace, wide bandgap (>1.7 eV) metal-halide perovskites (MHPs) are becoming a major focus of academic and industrial photovoltaic research. Compared to their lower bandgap (≤1.6 eV) counterparts, these types of perovskites suffer from higher levels of non-radiative losses in both the bulk material and in device configurations, constraining their efficiencies far below their thermodynamic potential. In this work, we investigate the energy losses in methylammonium (MA) free high-Br-content wide bandgap perovskites by using a combination of THz spectroscopy, steady-state and time-resolved photoluminescence, coupled with drift-diffusion simulations. The investigation of this system allows us to study charge-carrier recombination in these materials and devices in the absence of halide segregation due to the photostabilty of formamidinium-cesium based lead halide perovskites. We find that these perovskites are characterised by large non-radiative recombination losses in the bulk material and that the interfaces with transport layers in solar cell devices strongly limit their open-circuit voltage. In particular, we discover that the interface with the hole transport layer performs particularly poorly, in contrast to 1.6 eV bandgap MHPs which are generally limited by the interface with the electron-transport layer. To overcome these losses, we incorporate and investigate the recombination mechanisms present with perovskites treated with the ionic additive 1-butyl-1-methylpipiderinium tetrafluoroborate. We find that this additive not only improves the radiative efficiency of the bulk perovskite, but also reduces the non-radiative recombination at both the hole and electron transport layer interfaces of full photovoltaic devices. In addition to unravelling the beneficial effect of this specific treatment, we further optimise our solar cells by introducing an additional LiF interface treatment at the electron transport layer interface. Together these treatments enable MA-free 1.79 eV bandgap perovskite solar cells with open-circuit voltages of 1.22 V and power conversion efficiencies approaching 17%, which is among the highest reported for this material system.

Received 25th August 2021,
Accepted 20th December 2021

DOI: 10.1039/d1ee02650j

rsc.li/ees

[a] *Department of Physics, University of Oxford, Clarendon Laboratory, Parks Road, Oxford, OX1 3PU, UK. E-mail: Pietro.caprioglio@physics.ox.ac.uk, henry.snaith@physics.ox.ac.uk*
[b] *Institute of Physics and Astronomy, University of Potsdam, Karl-Liebknecht-Str. 24-25, D-14476 Potsdam-Golm, Germany*
[c] *Helmholtz-Zentrum Berlin für Materialien und Energie GmbH, Berlin 12489, Germany*
[d] *Institut für Physik & IRIS Adlershof, Humboldt-Universitat zu Berlin, Berlin 12489, Germany*
[e] *Young Investigator Group Perovskite Tandem Solar Cells, Helmholtz-Zentrum Berlin für Materialien und Energie GmbH, Kekuléstraße 5, Berlin 12489, Germany*
[f] *Institute for Advanced Study, Technical University of Munich, Lichtenbergstrasse 2a, D-85748 Garching, Germany*

† Electronic supplementary information (ESI) available. See DOI: 10.1039/d1ee02650j

‡ These authors contributed equally.

Broader context

Photovoltaics (PV) are beginning to play a key role in the world's transition to sustainable energy production, but the speed and scale of their adoption will depend strongly on the power conversion efficiencies of PV modules. Metal halide perovskites, owing to their relatively facile fabrication and broadly tuneable bandgap, are extremely promising candidates for implementation as the top cell in tandem photovoltaic technologies, which promise to deliver power conversion efficiencies in excess of 30%. In the tandem device configuration, the perovskite top cell requires a wider bandgap (1.7–1.8 eV) compared to their single-junction counterparts (1.2–1.6 eV). However, these wide bandgap perovskites are limited by their relatively poor photovoltaic performance, compared to their lower bandgap counterparts, and finding routes to deliver both enhanced efficiency and stability are key to enabling commercially viable technology. Recently, it was reported that the addition of an ionic salt (1-butyl-1-methylpipiderinium tetrafluoroborate) to the perovskite material helps to significantly enhance the stability of the perovskite solar cell with a concomitant boost in efficiency. The stability of these perovskite materials can be further enhanced by careful choice of the precursor components, in particular the elimination of methylammonium (MA) from the crystal lattice. An in-depth investigation of the working mechanisms of these MA-free wide bandgap perovskites, notably in terms of energy losses, has been lacking, preventing a complete understanding and improvement of solar cells based on these materials. In this work, we study the charge-carrier recombination behaviour in wide bandgap perovskite thin films and full PV devices, and rationalise how the ionic additive improves the photovoltaic performance, both by studying neat materials and full photovoltaic devices. Using this knowledge, we fabricate state-of-the-art PV devices and as such, this work provides important insights into the physics of wide bandgap perovskite devices and their optimisation, providing essential knowledge for the successful implementation of tandem solar cells based on metal halide perovskites.

Introduction

During the last decade, metal halide perovskite solar cells have experienced an unprecedented rise in power conversion efficiency (PCE) which now exceeds 25% in single-junction cells, approaching the record efficiency of crystalline silicon.[1] This remarkable development can be explained by the impressive optoelectronic properties of these perovskites, including long charge-carrier diffusion lengths, high absorption coefficients and low levels of electronic disorder, quantified *via* low Urbach energies.[2–6] These properties, along with the relative ease of manufacturing perovskite thin films and widely tuneable bandgap, make metal halide perovskite solar cells a highly attractive prospect for commercialisation.[4,7,8] Importantly, the bandgap energies practically achievable make this technology suitable for multijunction architectures, either in combination with Si or low-bandgap perovskite sub cells.[9,10] However, despite over 29.5% efficiency having already been demonstrated for perovskite-on-silicon tandems, the wider bandgap perovskite top cells still contain many more fundamental losses than their lower bandgap single junction counterparts. For example, wide bandgap (WBG) perovskites ($E_g > 1.7$ eV), essential for tandem applications, suffer from severe open-circuit voltage (V_{OC}) losses.[11] Despite recent progress, the mechanisms that cause the wide bandgap materials to underperform as compared to the lower bandgap materials are still not fully understood.[11]

Commonly, high-efficiency wide-bandgap perovskites are prepared by tuning the halide ratio from I to Br on the X site of the perovskite crystal lattice, ABX_3.[4,7] As such, a wide range of bandgaps from $\sim$1.5 to $\sim$2.3 eV can be achieved, while the X-site is varied from triiodide to tribromide for the lead-based perovskites.[7] Importantly, in multijunction tandem devices, *i.e.* in perovskite-on-Si or perovskite-on-perovskite device configurations, bandgaps of $\sim$1.7 eV and $\sim$1.8 eV respectively are required to ensure that the sub-cells are current-matched while still producing the highest voltage and hence maximising efficiency.[12,13] However, to reach such bandgaps, a critical Br content ($\sim$20%) is surpassed after which the perovskite material can exhibit phase instability under illumination, undergoing segregation of the halide species.[14–17] This segregation is particularly severe for perovskites containing methylammonium (MA) on the A-site.[17] Importantly, after a certain ratio of Br is surpassed, the V_{OC} of these devices saturates at a value of *ca.* 1.2 V.[18] In early studies, this led to the conclusion that the formation of low bandgap I-rich domains is the main factor limiting the V_{OC} in solar cells featuring a higher concentration of Br.[14,18–20] However, it has been recently clarified that the low V_{OC}s observed in wide bandgap perovskites are predominantly caused by a low radiative efficiency of the initial wide bandgap phase and strong non-radiative recombination at the interfaces with the charge transport layers.[11,21,22] As such, it is important to understand how the conduction and valence bands of the wide bandgap perovskite align with the energy levels of transport layers which are commonly used for perovskites with a narrower bandgap. It has been shown that good energetic alignment between the perovskite and the transport layers is crucial to achieving high V_{OC} and exploiting the radiative potential of the neat semiconductor.[23,24]

Another key issue for perovskite photovoltaics is their long-term stability. It has been shown that the longevity of perovskite solar cells (PSCs) can be ameliorated by eliminating MA from the crystal lattice.[25–27] In addition to that, it has recently been reported that incorporating ionic additives (IAs) into the perovskite precursor solution can substantially enhance the lifetime of PSCs.[10,28] One such additive, 1-butyl-1-methylpiperidinium tetrafluoroborate ($[BMP]^+[BF_4]^-$) was shown to effectively act as defect passivating agent concomitantly enhancing the device stability, contrary to many common surface passivation techniques which are not suitable for long-term operational stability.[10,28–30] However, despite these impressive improvements, the effects of this approach on the recombination mechanisms are yet to be understood.

In this work, we focus on MA-free, $FA_{0.83}Cs_{0.17}Pb(I_{0.6}Br_{0.4})_3$, wide bandgap perovskite solar cells, both with and without IA modification, to investigate the non-radiative losses in state-of-the-art wide bandgap systems that are unaffected by halide phase segregation. Through photoluminescence quantum yield (PLQY) measurements and quasi-Fermi level splitting (QFLS) analysis on complete cells, partial device stacks and

neat materials, we quantify and pinpoint the origin of the non-radiative losses in devices based on WBG perovskites. Interestingly, compared to 1.6 eV bandgap perovskites, despite the absence of phase segregation, wide bandgap perovskites are generally characterised by larger non-radiative recombination in the neat material, setting their QFLS far below their thermodynamic limit. Additionally, both the hole and electron transport layers (HTL and ETL respectively), induce severe interface non-radiative recombination, resulting in rather limited V_{OC}. Using time-resolved photoluminescence spectroscopy (TRPL) studies, we calculate that that the IA reduces the surface recombination velocity (SRV) at each interface by approximately one order of magnitude. We find the SRV at the perovskite/C60 interface can be further reduced by the incorporation of a 1 nm thick LiF interlayer. Lastly, combining photoemission spectroscopy measurements and drift-diffusion simulations, we rationalise the crucial role of the energetic alignment between the perovskite semiconductor and the charge-transport layers in wide bandgap systems. With this understanding, we fabricate high efficiency 1.79 eV PSCs exhibiting PCEs approaching 17% with a V_{OC} of 1.22 V, which is among the highest reported for MA-free wide bandgap PSCs.[31–35] Furthermore, we identify that new transport layers are crucial to harness the full performance potential of these MA-free wide bandgap perovskites.

Results and discussion

Bulk optoelectronic properties

In this work, we use the MA-free formamidinium-caesium ($FA_{0.83}Cs_{0.17}Pb(I_{0.6}Br_{0.4})_3$) based perovskite first developed by McMeekin *et al.*,[4] which has a wide bandgap of $\sim$1.8 eV when processed *via* the anti-solvent quenching method. We chose this material due to its high stability and suitability for implementation in perovskite-on-perovskite tandem photovoltaic devices. To establish the impact of the ionic additive on the optoelectronic properties of $(FA_{0.83}Cs_{0.17})Pb(I_{0.6}Br_{0.4})_3$, a thorough spectroscopic characterisation of control and IA modified thin films was carried out. The absorption coefficient, α, of control and IA modified thin films is very similar for both samples and is shown in Fig. S1 (ESI†). In line with this, the similarity of the X-ray diffraction (XRD) patterns (Fig. S2, ESI†) of both samples demonstrates the negligible effect of the IA on the average crystallinity of the perovskite thin films.

To delve into the effect of the ionic additive on the charge-carrier dynamics within the bulk of the perovskite semiconductor, time-resolved photophysical spectroscopic studies were performed. In such measurements, perovskite thin films are photoexcited by laser pulses. Following an excitation pulse, the charge carrier concentration, n, within the perovskite semiconductor can be accurately described by the differential eqn (1)[36]

$$\frac{dn}{dt} = -k_1 n - k_2 n^2. \quad (1)$$

t is the time following the excitation pulse, k_1 is the monomolecular recombination rate related to first-order non-radiative trap-mediated recombination, k_2 is the bimolecular recombination rate describing radiative second-order band-to-band recombination within the perovskite semiconductor, and we have neglected higher-order (Auger) recombination and assumed equal concentrations of electrons and holes.

To investigate the intrinsic properties of the perovskite thin films, optical-pump terahertz-probe spectroscopy studies were performed. This technique does not require metallic electrodes and allows for investigation of the optoelectronic properties of the thin films, such as charge-carrier mobility and bimolecular (radiative) recombination, on picosecond timescales. This allows us to assess the charge-carrier dynamics of isolated perovskite thin films without the influence of any transport layers. The THz photoconductivity transients for control and IA modified thin films are shown in Fig. 1a and Fig. 1b, respectively. Numerical fits to the measured transient photoconductivity decays allow for the extraction of the bimolecular charge-carrier recombination constant k_2 (Auger recombination was neglected, as it was found to contribute negligibly at the charge-carrier densities investigated here, full details are provided in the ESI†). The extracted value k_2 is found to be unchanged with the addition of the ionic additive (values of 0.50 ± 0.06 and $0.52 \pm 0.05 \times 10^{-10}$ cm^3 s^{-1} for control and IA modified samples respectively), implying little change in the fundamental electronic structure of the material with the addition of the IA.[37] These values are in line with values previously measured for mixed-cation lead mixed-halide perovskites.[38,39] However, we note that they are underestimates of the actual intrinsic values of k_2 owing to the large thickness of the thin films measured here ($>$500 nm), which leads to a substantial role for charge-carrier diffusion and photon reabsorption which masks the intrinsic value of the bimolecular recombination rate constant.[40] Concomitantly, we find that the charge-carrier mobilities are high in both control and treated films, in excess of 32 cm^2 V^{-1} s^{-1}. These values are substantially higher than values reported in the literature for similar Br contents, approaching values measured for triiodide perovskites, demonstrating the high quality of our control and IA treated thin-films.[39,41–43] Nevertheless, considering that these measurements are short-range mobilities, it should be noted that these values represent upper limits of the effective mobility (or short-range intra-grain mobilities).[44] Overall, the absorption and OPTP measurements thus show us that the optical absorption, charge-carrier mobility and bimolecular (radiative) recombination rates are unaffected by the inclusion of the IA.

We now turn our attention to the extrinsic properties of these MA-free WBG perovskites. Time-resolved PL measurements were carried out to study the trap-assisted recombination regime in these materials. Transient decays of PL, measured using time-correlated single photon counting (TCSPC), are shown in Fig. 1c and d for control and IA-modified thin-film samples respectively. We fit the low excitation fluence transients (16 nJ cm^{-2}) with a stretched exponential,[45,46] from which we extract the monomolecular recombination rate constant (k_1) (details provided in the ESI†). We observe more than a two-fold reduction (from $k_1 = 1.0 \pm 0.1 \times 10^7$ s^{-1} to $k_1 = 0.39 \pm 0.04 \times 10^7$ s^{-1}) with the inclusion of the IA (Fig. S3, ESI†), indicating reduced trap-mediated recombination. Due to the lower value of k_1 in the IA treated film, using the optical-pump terahertz-probe mobilites, we estimate that the diffusion length is enhanced from 2.8 μm to 4.8 μm. Details of this calculation are

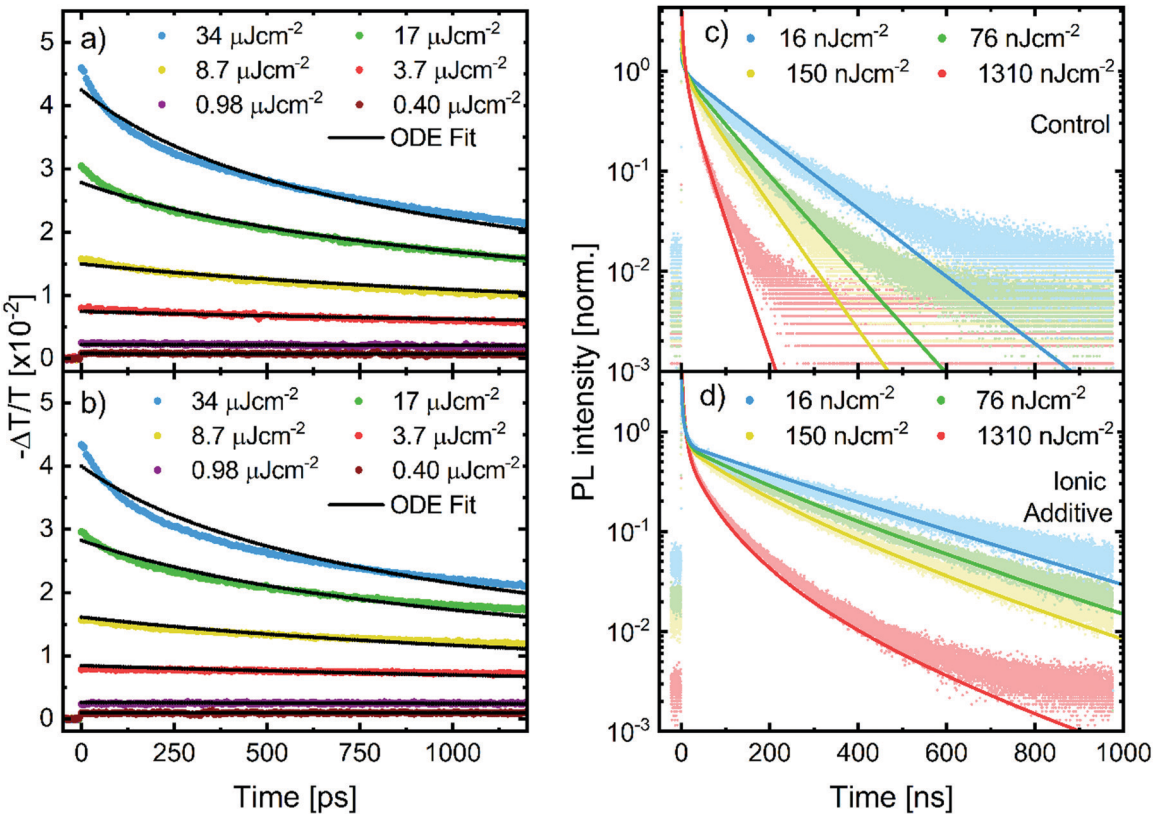

Fig. 1 Photophysical data for control (top row) and ionic additive (bottom row) samples on quartz substrates. (a, b) Optical-Pump Terahertz-Probe transient photoconductivity decays at fluences of 34, 17, 8.7, 3.7, 0.98, 0.40 μJ cm^{-2} (blue, green, yellow, red, purple, brown dots respectively) for control and IA modified samples respectively. Fitted numerical solutions to an ODE are shown as black lines (see the ESI† for details). (c and d) Time-resolved PL transients measured using time correlated single photon counting at fluences of 16, 76, 155 and 1310 nJ cm^{-2} (blue, green, yellow and red dots respectively) measured using pulsed (1 MHz repetition rate) excitation at 398 nm on the same samples as for the THz measurements. The data is normalised to the value at 10 ns following the laser pulse to allow for better visualisation. The solid lines are fits to the decays using the model described in detail in the ESI.† Diffusion was modelled for the first 20 ns (the charge-carrier profile was uniform throughout following this time). The result of the model without diffusion can be seen in Fig. S5 (ESI†).

presented in the ESI.† Both these values are substantial and, as such, the devices based on this material are unlikely to be limited by the diffusion lengths of the charge carriers.

To better understand the impact of the ionic additive upon the charge-carrier dynamics, we investigated the fluence dependence of the TCSPC PL transients. As observed in Fig. 1c and d, the PL decays recorded for the control sample are characterised by stretched dynamics and a more substantial shortening of lifetimes with increasing excitation fluence, in comparison to the ionic additive modified sample. We are able to explain this behaviour using a basic recombination model, discussed below, which reveals that the IA preferentially passivates traps for one charged species, greatly reducing trap-mediated recombination in the bulk perovskite.

If the dynamics were described by a simple recombination model, eqn (1), the control sample would require an order of magnitude higher value of k_2, as shown in Fig. S4 (ESI†). Our OPTP measurements, discussed above, show that this cannot be the case owing to the similarity of the THz transients in Fig. 1a and b, which give near identical values of the bimolecular recombination rate. Instead, we propose that the lower excitation density and higher repetition rate in the TCSPC measurements (1 MHz as opposed to 5 kHz in the OPTP experiment) influence the charge-carrier dynamics significantly, notably by altering the amount of trapped charge carriers that 'carry over' from one excitation pulse to the next (see ESI† for more detail). Given the long lifetimes of trapped carriers in lead halide perovskite semiconductors,[47] the shorter time period between photoexcitation pulses results in trap filling and population build-up. We investigate the influence of this higher repetition rate by employing a model in which the electron and hole first-order decay rates can vary, as previously implemented,[48] whilst also including the effect of diffusion to account for the rapid early time decay, seen in previous studies.[49] (More details of the model are provided in the ESI.†)

The dark solid lines in Fig. 1c and d show the modelled PL dynamics, implementing diffusion effects, for the control and IA modified samples respectively, which accurately describes the fluence-dependence of the experimental data. Importantly, such an agreement is reached without changes to the effective bimolecular recombination rate. The difference between the control and ionic additive films results from the unbalanced electron–hole trapping dynamics in the control sample and the consequent build-up of a charge-carrier population owing to the 1 MHz repetition rate of the photoexcitation. The lifetimes of electrons and holes for the control and IA modified samples

are presented in Fig. S7 (ESI†), and the corresponding remnant charge-carrier population at the time of arrival at the next pulse in Fig. S8 (ESI†). We confirm the role of trap-filling by conducting repetition rate dependent TCSPC measurements, Fig. S9 (ESI†), finding shorter lifetimes in the control sample for less frequent excitation pulses. In contrast, the lifetime for the IA modified sample was found to be independent of the repetition rate. The dynamics of the IA sample can be accurately modelled with balanced trapping rates, clearly identifying the role of the IA in passivating traps associated with one species, leading to the balanced-trapping dynamics and longer lifetimes evident in Fig. 1d. We support our model by performing fluence-dependent TCSPC with a slower repetition rate, Fig. S10 (ESI†), which allows more time between excitation pulses for traps to depopulate. Crucially, the PL transients of the control perovskite are best reproduced with unbalanced trap-mediated recombination rates for electrons and holes, whereas the PL transients of the IA sample can be very accurately reproduced with balanced trapping rates. Therefore, even when the role of trap-filling and population build up is reduced due to the extended time between pulses, our model appears to be appropriate. We cannot identify the specific nature of the trap species which is passivated by the IA from our studies here. However, the role of this same passivation molecule upon inhibiting photochemical degradation, which is considered to proceed *via* hole-trapping on Iodide interstitials,[10] and recent studies showing that hole-traps are prevalent at non-radiative recombination sites,[50] is consistent with hole-traps being predominantly passivated by this IA.

Our spectroscopic analysis of the optoelectronic properties of the bulk material demonstrates that IA incorporation reduces the non-radiative recombination losses within the bulk material without altering any of the fundamental structural, optical and electronic properties of the perovskite semiconductor.

Interface recombination

To quantify the effect of the IA on the interfacial recombination in partial device stacks we carried out photoluminescence quantum yield (PLQY) measurements. We performed these measurements on both glass substrates, to assess recombination in the bulk material, as well as on partial device stacks to determine to degree of interfacial recombination at each charge transport layer (CTL)/perovskite interface. As can be seen in Fig. 2a, the isolated control perovskite on glass (grey symbols) suffers from significant non-radiative losses achieving a PLQY of only 0.2%. This is consistent with previous studies and below values usually achievable in MA-free 1.6 eV-bandgap materials.[11,21,22,51–53] Given that our samples do not show phase segregation (discussed later), this indicates that perovskites comprising a higher Br content exhibit a large degree of non-radiative losses, possibly as the result of a higher density of traps in the initial mixed phase.[11,21,22,51–53] When either the HTL or the ETL are attached, the PLQY is significantly reduced owing to strong interfacial recombination. Interestingly, here the losses at the HTL interface are larger compared with the ETL interface, contrary to 1.6 eV bandgap perovskites using the same transport layers where the majority of the non-radiative recombination originates at the ETL interface.[21,23,49] Such a scenario might originate from the substantially different energetics that these perovskites may present in conjunction with the transport layers.[23,24] Importantly, when the ionic additive $[BMP]^+[BF_4]^-$ is incorporated in the perovskite, the PLQY is enhanced not only in the neat material, denoting a reduction of trap-assisted recombination in the bulk, as discussed earlier, but also at both the HTL and the ETL interfaces, Fig. 2a. This key finding highlights how despite the IA being added to the precursor solution, its effects are strongly visible at the perovskite/transport layer interfaces. Accordingly, the QFLS of the IA treated samples are also enhanced, demonstrating the possibility of high open-circuit voltages in full photovoltaic devices.[23,54,55] The improvement of the bulk perovskite observed following IA incorporation can originate from an effective reduction of trap densities, either by passivation of defects or by influencing the crystallisation process. On the other hand, the increase in QFLS when either transport layer is attached denotes that, even though the IA is incorporated directly in the bulk material, this additive may help to form a more ideal interface between the perovskite and each transport layer, either providing a better energetic alignment or by reducing the trap density at the interface.

To understand the influence of IA incorporation on the interfacial recombination kinetics, we measured the transient decay of the photoluminescence of partial device stacks using TCSPC. We investigated quartz/PTAA/perovskite (HTL stack) and quartz/perovskite/(LiF)/C60 (ETL stack) samples. The fluence-dependent PL transients, and corresponding differential lifetime, for each of these conditions are presented in Fig. S11–S14 (ESI†). In our investigation, we illuminated the HTL stack from the perovskite side, and the ETL stack from the quartz side. This ensures there is no parasitic absorption in the transport layer which would make further analysis challenging. The PL transients corresponding to the lowest excitation fluence (16 nJ cm^{-2}) for HTL and ETL stacks are shown in Fig. 2c and d respectively. We fit the decays using a double exponential (details provided in the ESI†) and show them with dark lines. The transient PL of the half stacks is influenced by several factors. In addition to charge-carrier recombination within the perovskite itself, charge transfer to the CTL becomes important, as does interfacial recombination between the majority carrier in the CTL with the minority carrier in the perovskite.[46,56] To disentangle these processes we define a differential lifetime which is given by

$$\tau_{\mathrm{diff}}(t) = \left(\frac{\mathrm{d}\ln(\varphi(t))}{\mathrm{d}t}\right)^{-1}, \qquad (2)$$

where $\varphi(t)$ is the photon flux. To perform this analysis, we fit the PL transients with a double exponential, since it accurately reproduces the PL transient, and take the numerical derivative of this fit, to determine τ_{diff}. We demonstrate the applicability of this fitting in Fig. S15 (ESI†). As can be seen in Fig. 2e and f, the lifetimes reach a plateau at large delay time. The initial rise at short delay times is attributed to charge transfer into the transport layers, whereas the longer lifetime is dominated by interface recombination.[46,56] As is evident in Fig. 2e and f, the incorporation

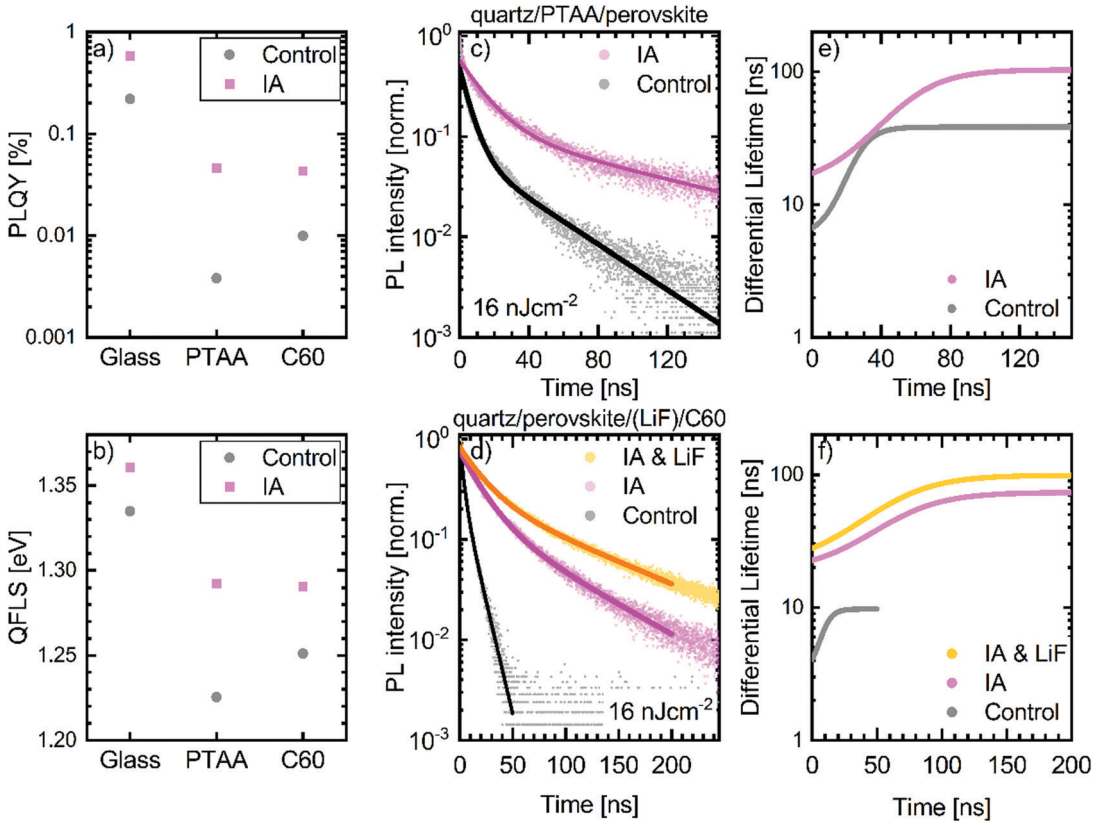

Fig. 2 Interfacial recombination analysis. (a) Photoluminescence quantum yield (PLQY) for isolated perovskite thin films on glass (labelled glass), a half device stack ITO/PTAA/PFN/perovskite (labelled PTAA) and glass/perovskite/C60 (labelled C60) for control (grey symbols) and IA modified (pink symbols). (b) The quasi-Fermi level splitting (QFLS) of the same samples calculated from the PLQY presented in (a) (details provided in the ESI†). (c) Time correlated single photon counting (TCSPC) decays for quartz/PTAA/perovskite samples with control (grey symbols) and IA modified (pink symbols) perovskites. The samples were illuminated from the perovskite side with a 398 nm laser at a fluence of 16 nJ cm^{-2}. The dark curves are double-exponential fits to the PL transients. (d) TCSPC decays for quartz/perovskite/(LiF)/C60 samples with control (no LiF, grey symbols) and IA modified (pink symbols) perovskite and IA modified perovskite with a LiF interlayer before the C60 (orange symbols). The samples were illuminated from the quartz side with a 398 nm centre wavelength laser at a fluence of 16 nJ cm^{-2}. The dark curves are double-exponential fits to the PL transient. (e and f) The differential lifetime $\tau_{diff}(t)$ calculated using eqn (2) for the PL transients presented in (c and d) respectively.

of the IA significantly enhances the differential lifetime at large delay times, indicative of reduced interface recombination. This agrees with our PLQY measurements where we demonstrated reduced non-radiative recombination at each charge transport layer with the IA present under steady-state conditions. Moreover, to investigate the possibility of reducing the interface recombination further, we implemented an ultra-thin (~1 nm) LiF interlayer between the perovskite and ETL as previously reported.[49,57,58] As expected, when LiF is included between the IA-modified perovskite thin film and the C60, the differential lifetime is further enhanced. To quantify the influence of LiF alone, we compare the PL transients of a control perovskite/LiF/C60 sample and an IA/C60 sample. As can be seen in Fig. S16 (ESI†), while the LiF interlayer does reduce the interfacial recombination, the IA treatment alone is more effective.

The lifetimes extracted from PL transients above (τ_{eff}) will be governed by both bulk and surface recombination according to the relation[59]

$$\frac{1}{\tau_{eff}} = \frac{1}{\tau_{bulk}} + \frac{1}{\tau_{surface}}. \quad (3)$$

We have determined the effective lifetime with the transport layers present in Fig. 2e and f, and the ''bulk lifetime'' when the transport layers are absent, from the fitting in Fig. 1c and d. Combining these values allows us to calculate the lifetime associated with recombination at the perovskite/CTL heterojunctions. If we assume that the recombination at the perovskite/CTL interface is far greater than at the perovskite/quartz or perovskite/air interfaces, we can express the surface lifetime as[49,59,60]

$$\tau_{surface} = \frac{d}{SRV} + \frac{4}{D}\left(\frac{d}{\pi}\right)^2, \quad (4)$$

where d is the sample thickness, D is the diffusion coefficient and SRV is the surface recombination velocity. We determine D using the Einstein relation $D = \mu k_B T/q$, where k_B is Boltzmann's constant, T the absolute temperature and μ the mobility obtained in the THz spectroscopy measurements (details in the ESI†). It is therefore possible for us to estimate the surface recombination velocity at each interface, which we display in Table 1.

For the control sample, the value of the SRV at the fullerene interface is comparable to values reported in the literature for narrower bandgaps,[60] but the SRV at the PTAA interface is substantially higher compared to literature values usually reported for ~1.6 eV bandgap perovskites.[49,60] This correlates

Table 1 Lifetimes extracted from TCSPC measurements of at 16 nJ cm^{-2} for the HTL and ETL stack. The SRV was calculated according to eqn (4). The bulk lifetimes used were 450 ns and 900 ns for control and IA modified samples respectively

Condition	Sample	Illumination side	τ_{eff} (ns)	SRV (cm s^{-1})
Control	HTL stack	Perovskite	38	1300
IA	HTL stack	Perovskite	100	450
Control	ETL stack	Quartz	10	5600
IA	ETL stack	Quartz	73	640
IA & LiF	ETL stack	Quartz	99	450

with our PLQY data and shows again that the PTAA interface performs relatively poorly in the control samples for these wide bandgap materials, as we show in Fig. 2a and b. Accordingly, we see that IA modification results in substantially reduced SRVs as compared to the control system in the same stack configuration. A large beneficial effect from the IA is observed at the C60 interface, where the SRV is reduced by close to one order of magnitude. As expected, the addition of LiF helps to reduce the SRV value even further to as low as 450 cm s^{-1}. This value is among the lowest reported for MA-free perovskites.[61] This is particularly impressive since our measurements were performed on perovskite films in contact with a CTL – known to induce significant non-radiative recombination as discussed earlier.[62]

This reduction of SRV and enhanced radiative efficiency is extremely promising for corresponding photovoltaic device performance.

Photovoltaic device performance

To corroborate our study on the recombination mechanisms in wide bandgap perovskites thin films, we implement these materials in a p–i–n device architecture. Inverted p–i–n device architectures have numerous advantages over their n–i–p counterparts including reduced hysteresis, low temperature processability, and consequent suitability for silicon tandem technologies.[63,64] The device architecture, shown in Fig. 3a, comprises PTAA as the hole transport layer which is coated with an ultra-thin layer of PFN-Br onto which the perovskite layer is deposited. The solar cell is then finished by evaporating thin LiF interlayer (depending on the device type), C60 as the electron transport layer, BCP (bathocuproine) and Cu as top electrode. The perovskite absorber is optionally modified by adding an optimised amount (0.5 mg mL^{-1}) of the ionic additive $[BMP]^{+}[BF4]^{-}$ to the precursor solution. The beneficial effects of the IA addition in devices are clearly visible in the exemplary JV-curves represented in Fig. 3b, where the V_{OC}, J_{SC} and FF are improved upon the incorporation of the ionic additive. We present the external quantum efficiency of representative devices in Fig. S17 (ESI†), and find the integrated current is in good agreement with the J_{sc} determined from the current–voltage characteristics. Additionally, with the addition of a LiF interlayer the FF is greatly enhanced and the V_{OC} also increases. The statistical summary of the three types of devices investigated in this work are presented in Fig. 3c. Here, the combination of the IA with a LiF interlayer allows us to reach V_{OC} of 1.22 V, FF above 80% and PCEs approaching 17%. We present the forward and reverse scans for each device type investigated, and the stabilised power output of these devices in Fig. S18 (ESI†). To compare with other published literature, in Fig. 3d we show that wide bandgap MA-free perovskites, especially in p–i–n architectures, are prone to modest power conversion efficiencies (PCE), due to larger V_{OC} losses compared to the radiative potential at the respective bandgap.

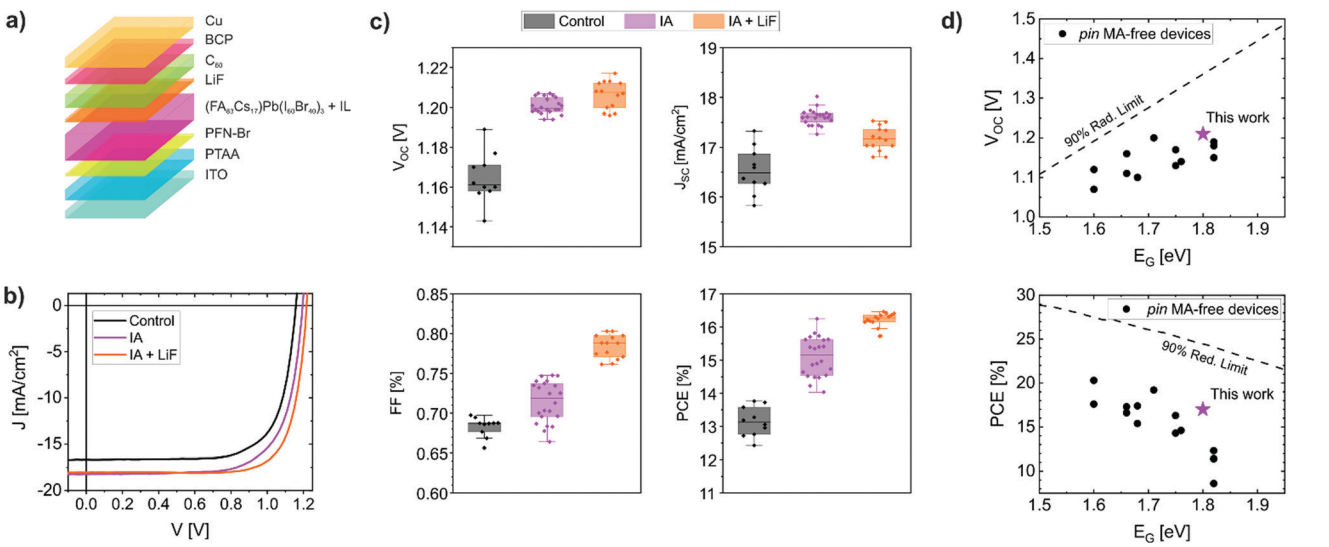

Fig. 3 Photovoltaic device performance. (a) Schematic of the device architecture utilised in this study. The device area was 0.06 cm^2. (b) Exemplary *JV* curves for the three types of devices investigated. (c) Statistical summary of reference FACs based perovskite solar cells (grey), IA modified devices (pink) and IA modified devices implementing a LiF interlayer (orange). The data points are overlapped onto the boxplots which show the median (central line), and the median of the upper and lower halves of the data (top and bottom lines of the box, respectively). The top and bottom whiskers are drawn to the highest/lowest data point within 1.5 times the interquartile range from the top and bottom of the box, respectively. (d) Literature comparison between our work (denoted with a star) and pin-type devices with MA-free perovskite solar cells. The dashed lines represent 90% of the radiative limit with respect to the bandgap energy.

While the V_{OC} and FF improvements are expected from devices showing increased radiative efficiency, as discussed previously, the enhancement of the short-circuit current density, evident in Fig. 3c, following IA modification is unexpected. Such an effect would imply either increased charge-carrier generation, extraction, or both. To rule out the possibility of increased charge-carrier generation, the optical constants of the perovskite, with and without the IA, were measured by ellipsometry (ESI†). As can be seen from Fig. S19 (ESI†), the optical constants of the control and IA-modified perovskite are extremely similar. As such we do not expect that there will be increased charge-carrier generation upon IA modification. This allows us to rule out any optical effect increasing the J_{sc}. It has recently been reported that mobile ions are an origin of short-circuit current density losses in perovskite solar cells.[65] Whilst determining the precise origin of the current density increase is beyond the scope of the current work, we suggest the increased J_{sc} may be due to reduced ionic mobility following IA modification. Such an effect would reduce the severity of current losses in these types of devices, manifesting as an increased J_{sc} as compared to the control devices.

Recombination analysis in full devices

To assess the effects of the IA and LiF on the recombination mechanisms in complete devices, we carried out two sets of illumination intensity-dependent measurements: illumination intensity-dependent PLQY and illumination intensity-dependent V_{OC} ($V_{OC}(I)$, I is the excitation intensity). The PLQY measurements were carried out on isolated thin films on glass substrates and the V_{OC} measurements on full devices. The PLQY measurements are used to determine the quasi-Fermi level splitting. As proposed in a recent publication, QFLS intensity-dependent measurements (QFLS(I)) can be used to reconstruct a pseudo *JV*-curve (*pJV*) for isolated perovskite thin films in the absence of the influence of charge transport layers (see ESI† for further details).[66] Such *pJV* curves therefore represent the maximum efficiency achievable with a particular absorber in the absence of interfacial recombination. In addition, it is possible to reconstruct a *pJV* curve using $V_{OC}(I)$ measurements on full devices. Thereby, such *pJV* curves are influenced exclusively by the recombination processes taking place in the device, at the interfaces or within the perovskite semiconductor, and not during charge-carrier transport. The advantage of this analysis approach is that through PLQY (and V_{OC}) measurements over a wide range of illumination intensities, we can estimate the effect of charge-carrier recombination on both the V_{OC} and the FF at the same time. This technique allows for the untangling of transport and recombination loss mechanisms within the devices, and ultimately facilitates estimating a potential efficiency of the single absorber or the device in absence of interfacial and/or transport losses. Notably, the intensity-dependent PL spectra (Fig. S20, ESI†), show no evidence of PL shift upon constant illumination and high illumination intensities, denoting the absence of phase segregation that is usually observed in MA-containing high Br content perovskites.[14,16,17,21]

In Fig. 4a–c, we compare the normal *JV* with the *pJV* of the same device (from $V_{OC}(I)$ measurements) and that of the bare absorber (from QFLS(I) measurements). From these data, it is possible to quantify and visualise the significance of non-radiative and transport losses of our different cells and materials. The losses are highlighted as the shaded purple and turquoise areas, respectively, between the different *JV* and *pJV* in Fig. 4a–c. These plots graphically demonstrate that the incorporation of the IA is effective at both reducing the recombination and charge-carrier transport losses in complete devices, and both losses are further reduced by the addition of LiF. This finding is in excellent agreement with our TCSPC analysis on the IA's effect on the bulk material and each interface between the perovskite and the CTLs. Additionally, in the case of an isolated thin film, this estimates the ideal case of a solar cell with zero interfacial losses. This highlights how this 1.79 eV (determined from the inflection point of the EQE) bandgap IA modified perovskite could potentially achieve a PCE of 23.17% if implemented in a fully optimised device, where all recombination and transport losses at interfaces and in the device are eliminated. We present the estimated device characteristics in Table 2.

In Fig. 4d, the ideality factor from the V_{OC} intensity dependence study is calculated and shows that the devices treated with IA and LiF exhibit larger ideality factors compared to the reference cell. These results are in line with a recent study and demonstrate the effective reduction of interface recombination upon optimisation, in agreement with the enhanced V_{OC} evident in Fig. 3c.[67] The LiF has a negligible effect on the QFLS in the absence of a transport layer, Fig. S21 (ESI†). This explains the similarity of the *pJV* curves for the IA and IA & LiF cases summarised in Table 2.

We summarise the impact of non-radiative losses on the radiative potential of our devices in Fig. 4e. Generally, this MA-free wide bandgap perovskite is characterised by a large degree of non-radiative losses (indicated in blue) compared to the radiative open-circuit voltage limit of 1.50 V present for a solar absorber with the optical properties of the neat material. This denotes strong non-radiative losses taking place in the neat perovskite absorber, possibly due to high density of traps, which are reduced by IA implementation. As discussed earlier, the contacting with the transport layers results in significant interfacial non-radiative losses (purple region) and therefore a further reduction in the V_{OC} and QFLS. Importantly, the QFLS of the full devices represents the maximum realistically achievable open-circuit voltage which is measured internally in the device's absorber. Interestingly, however, the externally measured V_{OC} of these devices lies substantially below these values, as indicated by the shaded turquoise region. We find here that IA and LiF treatments improve the QFLS of the full devices (including the metallic electrodes). Critically, they also improve the V_{OC} of the very same devices, but to a more significant degree than the improvement in QFLS. As a result, although not entirely eliminated, the mismatch between the QFLS and the V_{OC} is reduced with these treatments (shaded turquoise region in Fig. 4e). We proceed to investigate the origin of the remaining mismatch.

A mismatch between QFLS and V_{OC} has been previously attributed to an energetic misalignment between the perovskite and the CTLs in combination with interface recombination.[23,24] To investigate the origin of this loss in our devices, we conducted

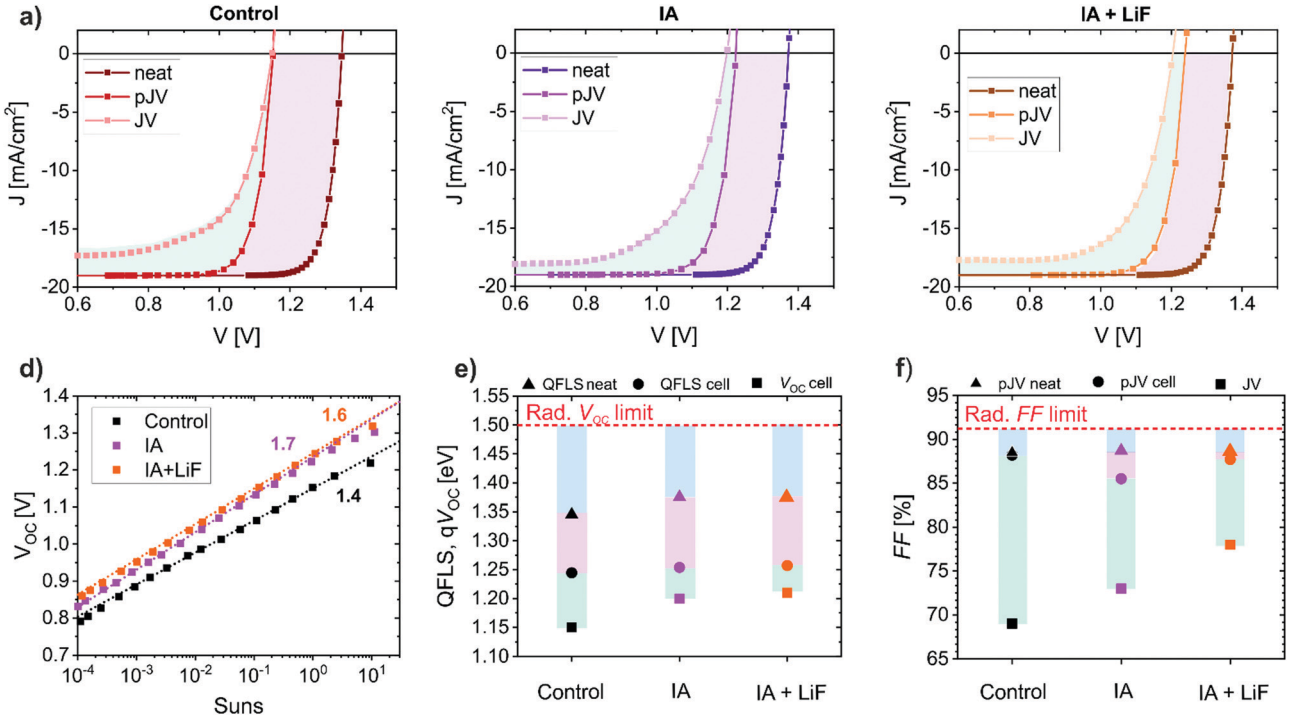

Fig. 4 Comparison between the measured *JV* curve of a solar cell and the reconstructed pseudo-*JV* curves from intensity dependent measurements on the same solar cell device and respective neat material. The results are shown in (a) for the reference perovskite, in (b) for the perovskite including IA, and in (c) with the additional addition of a LiF interlayer. In (a,b,c) the right-most curve is determined from QFLS(*I*) measurements of thin films on glass, and so represents a pseudo-*JV* curve with minimal interface recombination. The centre curve is derived from $V_{OC}(I)$ measurements on full devices, and represents a pseudo-*JV* curve with interfacial recombination, but in the absence of transport losses. The left-most curve is the *JV* curve of the same device measured on the solar simulator. (d) V_{OC} intensity-dependent measurements and ideality factors for solar cell devices implementing reference FACs, FACs including IA, and FACs with IA and additional LiF. (e) V_{OC} energy losses summary calculated from the samples and data presented in (a, b and c). (f) A summary of FF energy losses calculated from the samples and data presented in (a, b and c).

ultraviolet photoemission spectroscopy (UPS) measurements specifically probing the perovskite/C60 interfaces by performing multistep sequential deposition of C60 molecules, which are presented in Fig. S22 (ESI†). As such, we are able to reconstruct the energetics at these specific interfaces accurately, and the band diagrams derived from these measurements are presented in Fig. S22 (ESI†). Our UPS measurements highlight a misalignment between the conduction band of the perovskite and the lowest unoccupied molecular orbital of the C60 in all conditions investigated, despite the implementation of IA or LiF. Therefore, we conclude that the reduction of the QFLS-V_{OC} mismatch in these devices is not necessarily due to a better energetic alignment of the perovskite with the ETL. Such a reduction in the mismatch could be related to the partial specific resistances for electrons and holes at the CTL interfaces.[68] However, we observe that the Fermi level is shifted towards mid-gap upon IA modification, which may be due to a reduction in surface defects in line with our previous analysis.[69,70] Further discussion of the UPS measurements can be found in the ESI.† The finding of the energetic misalignment between the perovskite and the C60 is significant and sufficient to give rise to a QFLS-V_{OC} mismatch. However, we do not exclude the possibility of an additional energetic misalignment between the highest occupied molecular orbital (HOMO) of the PTAA and the perovskite valence band (VB). Since the PTAA HOMO is well-aligned with the VB of 1.6 eV perovskites, the shifting of the perovskite valence band away from vacuum as the Br content is increased is likely to induce an energetic misalignment at this interface for these wide bandgap perovskites.[24,71]

As shown in Fig. 4e, even for optimised devices utilising the combination IA and LiF, the V_{OC} measured in the device still lies more than 60 meV below the potentially achievable internal QFLS. Therefore, developing transport layers with better energetic alignment, or another approach to reduce the mismatch between

Table 2 Estimated PCE (in the absence of interfacial and/or transport losses) obtained from the *pJV* of cells and isolated thin films for the materials investigated in the study. The J_{SC} used here to estimate the efficiency potentials are calculated by assuming 95% of the thermodynamic limit corresponding to the bandgap

	Method	J_{sc} [mA cm^{-2}]	V_{OC} [V]	pFF [%]	pPCE [%]
Control	QFLS(*I*)	19	1.345	88.5	22.61
Control	$V_{OC}(I)$	19	1.156	88.2	19.37
IA	QFLS(*I*)	19	1.375	88.7	23.17
IA	$V_{OC}(I)$	19	1.22	85.5	19.81
IA & LiF	QFLS(*I*)	19	1.375	88.7	23.17
IA & LiF	$V_{OC}(I)$	19	1.23	87.7	20.5

internal and external voltage, would enable full exploitation of the radiative potential of the optimised perovskite and interfaces.

Moreover, this need for a new device architecture for MA-free wide bandgap perovskites is further highlighted in Fig. 4f. Therein, we find the pFFs determined from the isolated materials on glass for each condition lie extremely close to the radiative limit, indicating that recombination losses have a minimal impact on the FF of these materials. On the other hand, we see a significant difference between the pFF determined from the intensity-dependent V_{OC} measurements (presented in Fig. 4d) and the FF determined from the *JV* curves, indicating the carrier transport losses out of the device, are the main cause for FF loss in these devices. We find that, firstly the IA and then the LiF addition, successfully reduce the difference between the ideal "transport-free" FF and the FF measured in *JV* scans. However, this finding again highlights the need for improved charge transport layers for wide bandgap perovskite semiconductors.

To corroborate the combination of our findings and to better correlate this improved device performance with the spectroscopic characterisation performed earlier, drift-diffusion simulations were performed using SCAPS.[72] Importantly, we use values determined experimentally in our earlier analysis as input simulation parameters, including the bulk lifetimes and surface recombination velocities at each interface. Moreover, the energy alignment between the layers is informed by the photoemission spectroscopy results. A table of the input parameters can be found in Table S2 (ESI†). Our simulations were able to reproduce the photovoltaic device performance parameters well in all aspects apart from the enhanced short-circuit current density following IA modification, confirming the agreement of our loss analysis and recombination model from neat material and interfaces to full devices. We present the simulated *JV* curves in Fig. S23 (ESI†), which closely reproduce those measured on full photovoltaic devices. This demonstrates the validity of our earlier analysis, but highlights that understanding current losses in these p–i–n devices requires further investigation.

Conclusions

In this work, we have unravelled the origin of performance limitations in methylammonium-free p–i–n wide bandgap perovskite solar cells. We have demonstrated that these solar cells are limited by significant non-radiative recombination in the bulk material which is exacerbated by the attachment of both electron and hole transport layers. We further show that there is a large energetic misalignment between the perovskite and the charge transporting layers (CTLs). To overcome these limitations, we incorporated the ionic additive 1-butyl-1-methylpiperidinium tetrafluoroborate into the perovskite precursor solution which is known to substantially enhance the stability of PSCs but its influence on device performance was unclear. We found that the incorporation of this additive reduces non-radiative recombination within the bulk of the perovskite, as well as at each interface with the charge transporting layers. This passivation effect results in substantially reduced surface recombination velocities at these interfaces. We showed further that a thin LiF interlayer between the perovskite and the C60 further reduces the SRV. We implement this knowledge to fabricate high performance 1.79 eV band gap perovskite solar cells, which approach 17% PCE with a V_{OC} of 1.22 V. This is among the highest reported for MA-free WBG perovskite solar cells. We then performed a thorough recombination analysis in the full devices. We found that the combination of the ionic additive and LiF interlayer significantly reduce the transport losses in full devices, likely due to the substantially lower SRVs present at the interfaces in these devices. In addition, the V_{OC} sits below the QFLS of the full devices, which we attribute to energetic misalignment between the perovskite and the charge transporting layers. To recover this lost voltage, better alignment of transport layers is essential. Therefore, we suggest that new transport layers better suited for wide bandgap materials need to be implemented in addition to the IA treatment we report here.

Author contributions

Robert D. J. Oliver: conceptualisation, formal analysis, investigation, visualisation, writing – original draft; Pietro Caprioglio: conceptualisation, formal analysis, investigation, visualisation, writing – original draft; Francisco Peña-Camargo: formal analysis, investigation; Leonardo Buizza: formal analysis, investigation; Fengshuo Zu: formal analysis, investigation; Alexandra J. Ramadan: investigation, formal analysis, supervision; Silvia G. Motti: formal analysis; Suhas Mahesh: formal analysis, investigation; Melissa M. McCarthy: investigation; Jonathan H. Warby: investigation; Yen-Hung Lin: conceptualisation; Steve Albrecht: funding acquisition, supervision; Norbert Koch: funding acquisition, supervision; Laura M. Herz: funding acquisition, supervision; Michael B. Johnston: funding acquisition, supervision; Dieter Neher: funding acquisition, resources, supervision; Martin Stolterfoht: conceptualisation, supervision; Henry J. Snaith: conceptualisation, funding acquisition, resources, supervision.

Conflicts of interest

Henry Snaith is the founder and Chief Scientific Officer of Oxford Photovoltaics, a company commercialising perovskite photovoltaics.

Acknowledgements

This project received funding from Engineering and Physical Science Research Council (EPSRC) under EP/S004947/1, the Deutsche Forschungsgemeinschaft (DFG, German Research Foundation) – Project number 423749265 and 424709669 – SPP 2196 (SURPRISE and HIPSTER), the Federal Ministry for Economic Affairs and Energy within the framework of the 7th Energy Research Programme (P3T-HOPE, 03EE1017C). This project has received funding from the European Union's Horizon 2020 framework programme for research and innovation under grant agreement No 763977 of the PerTPV project and the

European Union's Horizon 2020 research and innovation program under Grant agreement no. 861985. RDJO would like to express his gratitude to the Penrose scholarship for funding his studentship. SM expresses gratitude to the Rhodes Trust. LRVB acknowledges funding from the EPSRC Centre for Doctoral Training in New and Sustainable Photovoltaics, and from the Oxford-Radcliffe scholarship. L. M. H. acknowledges support through a Hans Fischer Senior Fellowship from the Technical University of Munich's Institute for Advanced Study, funded by the German Excellence Initiative.

Notes and references

1 NREL Best Research Cell Efficiency Chart, https://www.nrel.gov/pv/assets/pdfs/best-research-cell-efficiencies-rev211117.pdf, Accessed July 2021.
2 S. D. Stranks, G. E. Eperon, G. Grancini, C. Menelaou, M. J. P. Alcocer, T. Leijtens, L. M. Herz, A. Petrozza and H. J. Snaith, *Science*, 2013, **342**, 341–344.
3 C. Wehrenfennig, G. E. Eperon, M. B. Johnston, H. J. Snaith and L. M. Herz, *Adv. Mater.*, 2014, **26**, 1584–1589.
4 D. P. McMeekin, G. Sadoughi, W. Rehman, G. E. Eperon, M. Saliba, M. T. Hörantner, A. Haghighirad, N. Sakai, L. Korte, B. Rech, M. B. Johnston, L. M. Herz and H. J. Snaith, *Science*, 2016, **351**, 151–155.
5 M. A. Green, A. Ho-Baillie and H. J. Snaith, *Nat. Photonics*, 2014, **8**, 506–514.
6 A. Sadhanala, F. Deschler, T. H. Thomas, S. E. Dutton, K. C. Goedel, F. C. Hanusch, M. L. Lai, U. Steiner, T. Bein, P. Docampo, D. Cahen and R. H. Friend, *J. Phys. Chem. Lett.*, 2014, **5**, 2501–2505.
7 G. E. Eperon, S. D. Stranks, C. Menelaou, M. B. Johnston, L. M. Herz and H. J. Snaith, *Energy Environ. Sci.*, 2014, **7**, 982.
8 H. J. Snaith, *Nat. Mater.*, 2018, **17**, 372–376.
9 G. E. Eperon, T. Leijtens, K. A. Bush, R. Prasanna, T. Green, J. T.-W. Wang, D. P. McMeekin, G. Volonakis, R. L. Milot, R. May, A. Palmstrom, D. J. Slotcavage, R. A. Belisle, J. B. Patel, E. S. Parrott, R. J. Sutton, W. Ma, F. Moghadam, B. Conings, A. Babayigit, H.-G. Boyen, S. Bent, F. Giustino, L. M. Herz, M. B. Johnston, M. D. McGehee and H. J. Snaith, *Science*, 2016, **354**, 861–865.
10 Y.-H. Lin, N. Sakai, P. Da, J. Wu, H. C. Sansom, A. J. Ramadan, S. Mahesh, J. Liu, R. D. J. Oliver, J. Lim, L. Aspitarte, K. Sharma, P. K. Madhu, A. B. Morales-Vilches, P. K. Nayak, S. Bai, F. Gao, C. R. M. Grovenor, M. B. Johnston, J. G. Labram, J. R. Durrant, J. M. Ball, B. Wenger, B. Stannowski and H. J. Snaith, *Science*, 2020, **369**, 96–102.
11 S. Mahesh, J. M. Ball, R. D. J. Oliver, D. P. McMeekin, P. K. Nayak, M. B. Johnston and H. J. Snaith, *Energy Environ. Sci.*, 2020, **13**, 258–267.
12 M. T. Hörantner and H. J. Snaith, *Energy Environ. Sci.*, 2017, **10**, 1983–1993.
13 G. E. Eperon, T. Leijtens, K. A. Bush, R. Prasanna, T. Green, J. T. W. Wang, D. P. McMeekin, G. Volonakis, R. L. Milot, R. May, A. Palmstrom, D. J. Slotcavage, R. A. Belisle, J. B. Patel, E. S. Parrott, R. J. Sutton, W. Ma, F. Moghadam, B. Conings, A. Babayigit, H. G. Boyen, S. Bent, F. Giustino, L. M. Herz, M. B. Johnston, M. D. McGehee and H. J. Snaith, *Science*, 2016, **354**, 861–865.
14 E. T. Hoke, D. J. Slotcavage, E. R. Dohner, A. R. Bowring, H. I. Karunadasa and M. D. McGehee, *Chem. Sci.*, 2015, **6**, 613–617.
15 A. J. Barker, A. Sadhanala, F. Deschler, M. Gandini, S. P. Senanayak, P. M. Pearce, E. Mosconi, A. J. Pearson, Y. Wu, A. R. Srimath Kandada, T. Leijtens, F. De Angelis, S. E. Dutton, A. Petrozza and R. H. Friend, *ACS Energy Lett.*, 2017, **2**, 1416–1424.
16 A. J. Knight and L. M. Herz, *Energy Environ. Sci.*, 2020, **13**, 2024–2046.
17 A. J. Knight, J. Borchert, R. D. J. Oliver, J. B. Patel, P. G. Radaelli, H. J. Snaith, M. B. Johnston and L. M. Herz, *ACS Energy Lett.*, 2021, 799–808.
18 E. L. Unger, L. Kegelmann, K. Suchan, D. Sörell, L. Korte and S. Albrecht, *J. Mater. Chem. A*, 2017, **5**, 11401–11409.
19 D. J. Slotcavage, H. I. Karunadasa and M. D. McGehee, *ACS Energy Lett.*, 2016, **1**, 1199–1205.
20 K. Suchan, A. Merdasa, C. Rehermann, E. L. Unger and I. G. Scheblykin, *J. Lumin.*, 2020, **221**, 117073.
21 F. Peña-Camargo, P. Caprioglio, F. Zu, E. Gutierrez-Partida, C. M. Wolff, K. Brinkmann, S. Albrecht, T. Riedl, N. Koch, D. Neher and M. Stolterfoht, *ACS Energy Lett.*, 2020, **5**, 2728–2736.
22 P. Caprioglio, S. Caicedo-Dávila, T. C.-J. Yang, C. M. Wolff, F. Peña-Camargo, P. Fiala, B. Rech, C. Ballif, D. Abou-Ras, M. Stolterfoht, S. Albrecht, Q. Jeangros and D. Neher, *ACS Energy Lett.*, 2021, **6**, 419–428.
23 P. Caprioglio, M. Stolterfoht, C. M. Wolff, T. Unold, B. Rech, S. Albrecht and D. Neher, *Adv. Energy Mater.*, 2019, **9**, 1901631.
24 M. Stolterfoht, P. Caprioglio, C. M. Wolff, J. A. Márquez, J. Nordmann, S. Zhang, D. Rothhardt, U. Hörmann, Y. Amir, A. Redinger, L. Kegelmann, F. Zu, S. Albrecht, N. Koch, T. Kirchartz, M. Saliba, T. Unold and D. Neher, *Energy Environ. Sci.*, 2019, **12**, 2778–2788.
25 B. Conings, J. Drijkoningen, N. Gauquelin, A. Babayigit, J. D'Haen, L. D'Olieslaeger, A. Ethirajan, J. Verbeeck, J. Manca, E. Mosconi, F. De Angelis and H. G. Boyen, *Adv. Energy Mater.*, 2015, **5**, 1–8.
26 S. N. Habisreutinger, D. P. McMeekin, H. J. Snaith and R. J. Nicholas, *APL Mater.*, 2016, **4**, 091503.
27 D. P. Nenon, J. A. Christians, L. M. Wheeler, J. L. Blackburn, E. M. Sanehira, B. Dou, M. L. Olsen, K. Zhu, J. J. Berry and J. M. Luther, *Energy Environ. Sci.*, 2016, **9**, 2072–2082.
28 S. Bai, P. Da, C. Li, Z. Wang, Z. Yuan, F. Fu, M. Kawecki, X. Liu, N. Sakai, J. T. W. Wang, S. Huettner, S. Buecheler, M. Fahlman, F. Gao and H. J. Snaith, *Nature*, 2019, **571**, 245–250.
29 Q. Jiang, Y. Zhao, X. Zhang, X. Yang, Y. Chen, Z. Chu, Q. Ye, X. Li, Z. Yin and J. You, *Nat. Photonics*, 2019, **13**, 460–466.

30 R. D. J. Oliver, Y.-H. Lin, A. J. Horn, C. Q. Xia, J. H. Warby, M. B. Johnston, A. J. Ramadan and H. J. Snaith, *ACS Energy Lett.*, 2020, **5**, 3336–3343.
31 K. A. Bush, K. Frohna, R. Prasanna, R. E. Beal, T. Leijtens, S. A. Swifter and M. D. McGehee, *ACS Energy Lett.*, 2018, **3**, 428–435.
32 T. Leijtens, R. Prasanna, K. A. Bush, G. Eperon, J. A. Raiford, A. Gold-Parker, E. J. Wolf, S. A. Swifter, C. C. Boyd, H.-P. Wang, M. F. Toney, S. Bent and M. D. McGehee, *Sustainable Energy Fuels*, 2018, **2**, 2450–2459, DOI: 10.1039/C8SE00314A.
33 Z. Li, T. H. Kim, S. Y. Han, Y. J. Yun, S. Jeong, B. Jo, S. A. Ok, W. Yim, S. H. Lee, K. Kim, S. Moon, J. Y. Park, T. K. Ahn, H. Shin, J. Lee and H. J. Park, *Adv. Energy Mater.*, 2020, **10**, 1–16.
34 Y. Wang, S. Gu, G. Liu, L. Zhang, Z. Liu, R. Lin, K. Xiao, X. Luo, J. Shi, J. Du, F. Meng, L. Li, Z. Liu and H. Tan, *Sci. China: Chem.*, 2021, **64**, 2025–2034, DOI: 10.1007/s11426-021-1059-1.
35 A. F. Palmstrom, G. E. Eperon, T. Leijtens, R. Prasanna, S. N. Habisreutinger, W. Nemeth, E. A. Gaulding, S. P. Dunfield, M. Reese, S. Nanayakkara, T. Moot, J. Werner, J. Liu, B. To, S. T. Christensen, M. D. McGehee, M. F. A. M. van Hest, J. M. Luther, J. J. Berry and D. T. Moore, *Joule*, 2019, **3**, 2193–2204.
36 C. Wehrenfennig, M. Liu, H. J. Snaith, M. B. Johnston and L. M. Herz, *Energy Environ. Sci.*, 2014, **7**, 2269–2275.
37 C. L. Davies, M. R. Filip, J. B. Patel, T. W. Crothers, C. Verdi, A. D. Wright, R. L. Milot, F. Giustino, M. B. Johnston and L. M. Herz, *Nat. Commun.*, 2018, **9**, 293.
38 W. Rehman, R. L. Milot, G. E. Eperon, C. Wehrenfennig, J. L. Boland, H. J. Snaith, M. B. Johnston and L. M. Herz, *Adv. Mater.*, 2015, **27**, 7938–7944.
39 W. Rehman, D. P. McMeekin, J. B. Patel, R. L. Milot, M. B. Johnston, H. J. Snaith and L. M. Herz, *Energy Environ. Sci.*, 2017, **10**, 361–369.
40 T. W. Crothers, R. L. Milot, J. B. Patel, E. S. Parrott, J. Schlipf, P. Müller-Buschbaum, M. B. Johnston and L. M. Herz, *Nano Lett.*, 2017, **17**, 5782–5789.
41 L. R. V. Buizza, T. W. Crothers, Z. Wang, J. B. Patel, R. L. Milot, H. J. Snaith, M. B. Johnston and L. M. Herz, *Adv. Funct. Mater.*, 2019, **29**, 1902656.
42 D. P. McMeekin, Z. Wang, W. Rehman, F. Pulvirenti, J. B. Patel, N. K. Noel, M. B. Johnston, S. R. Marder, L. M. Herz and H. J. Snaith, *Adv. Mater.*, 2017, **29**, 1607039.
43 L. M. Herz, *ACS Energy Lett.*, 2017, **2**, 1539–1548.
44 J. Lim, M. T. Hörantner, N. Sakai, J. M. Ball, S. Mahesh, N. K. Noel, Y.-H. Lin, J. B. Patel, D. P. McMeekin, M. B. Johnston, B. Wenger and H. J. Snaith, *Energy Environ. Sci.*, 2019, **12**, 169–176.
45 D. C. Johnston, *Phys. Rev. B: Condens. Matter Mater. Phys.*, 2006, **74**, 184430.
46 T. Kirchartz, J. A. Márquez, M. Stolterfoht and T. Unold, *Adv. Energy Mater.*, 2020, **10**, 1904134.
47 S. G. Motti, D. Meggiolaro, S. Martani, R. Sorrentino, A. J. Barker, F. De Angelis and A. Petrozza, *Adv. Mater.*, 2019, **31**, 1901183.
48 A. M. Ulatowski, A. D. Wright, B. Wenger, L. R. V. Buizza, S. G. Motti, H. J. Eggimann, K. J. Savill, J. Borchert, H. J. Snaith, M. B. Johnston and L. M. Herz, *J. Phys. Chem. Lett.*, 2020, **11**, 3681–3688.
49 M. Stolterfoht, C. M. Wolff, J. A. Márquez, S. Zhang, C. J. Hages, D. Rothhardt, S. Albrecht, P. L. Burn, P. Meredith, T. Unold and D. Neher, *Nat. Energy*, 2018, **3**, 847–854.
50 T. A. S. Doherty, A. J. Winchester, S. Macpherson, D. N. Johnstone, V. Pareek, E. M. Tennyson, S. Kosar, F. U. Kosasih, M. Anaya, M. Abdi-Jalebi, Z. Andaji-Garmaroudi, E. L. Wong, J. Madéo, Y.-H. Chiang, J.-S. Park, Y.-K. Jung, C. E. Petoukhoff, G. Divitini, M. K. L. Man, C. Ducati, A. Walsh, P. A. Midgley, K. M. Dani and S. D. Stranks, *Nature*, 2020, **580**, 360–366.
51 K. Schutt, P. K. Nayak, A. J. Ramadan, B. Wenger, Y. Lin and H. J. Snaith, *Adv. Funct. Mater.*, 2019, **29**, 1900466.
52 M. J. Trimpl, A. D. Wright, K. Schutt, L. R. V. Buizza, Z. Wang, M. B. Johnston, H. J. Snaith, P. Müller-Buschbaum and L. M. Herz, *Adv. Funct. Mater.*, 2020, **30**, 1–12.
53 J. S. W. Godding, A. J. Ramadan, Y. H. Lin, K. Schutt, H. J. Snaith and B. Wenger, *Joule*, 2019, **3**, 2716–2731.
54 R. T. Ross, *J. Chem. Phys.*, 1967, **46**, 4590–4593.
55 O. D. Miller, E. Yablonovitch and S. R. Kurtz, *IEEE J. Photovoltaics*, 2012, **2**, 303–311.
56 B. Krogmeier, F. Staub, D. Grabowski, U. Rau and T. Kirchartz, *Sustainable Energy Fuels*, 2018, **2**, 1027–1034.
57 J. Seo, S. Park, Y. Chan Kim, N. J. Jeon, J. H. Noh, S. C. Yoon and S. Il Seok, *Energy Environ. Sci.*, 2014, **7**, 2642–2646.
58 A. Al-Ashouri, E. Köhnen, B. Li, A. Magomedov, H. Hempel, P. Caprioglio, J. A. Márquez, A. B. Morales Vilches, E. Kasparavicius, J. A. Smith, N. Phung, D. Menzel, M. Grischek, L. Kegelmann, D. Skroblin, C. Gollwitzer, T. Malinauskas, M. Jošt, G. Matič, B. Rech, R. Schlatmann, M. Topič, L. Korte, A. Abate, B. Stannowski, D. Neher, M. Stolterfoht, T. Unold, V. Getautis and S. Albrecht, *Science*, 2020, **370**, 1300–1309.
59 A. B. Sproul, *J. Appl. Phys.*, 1994, **76**, 2851–2854.
60 J. Wang, W. Fu, S. Jariwala, I. Sinha, A. K.-Y. Jen and D. S. Ginger, *ACS Energy Lett.*, 2019, **4**, 222–227.
61 S. Jariwala, S. Burke, S. Dunfield, R. C. Shallcross, M. Taddei, J. Wang, G. E. Eperon, N. R. Armstrong, J. J. Berry and D. S. Ginger, *Chem. Mater.*, 2021, **33**, 5035–5044.
62 C. M. Wolff, P. Caprioglio, M. Stolterfoht and D. Neher, *Adv. Mater.*, 2019, **31**, 1902762.
63 H. J. Snaith, A. Abate, J. M. Ball, G. E. Eperon, T. Leijtens, N. K. Noel, S. D. Stranks, J. T. W. Wang, K. Wojciechowski and W. Zhang, *J. Phys. Chem. Lett.*, 2014, **5**, 1511–1515.
64 P. K. Nayak, S. Mahesh, H. J. Snaith and D. Cahen, *Nat. Rev. Mater.*, 2019, **4**, 269–285.
65 J. Thiesbrummel, V. M. Le Corre, F. Peña-Camargo, L. Perdigón-Toro, F. Lang, F. Yang, M. Grischek, E. Gutierrez-Partida, J. Warby, M. D. Farrar, S. Mahesh, P. Caprioglio, S. Albrecht, D. Neher, H. J. Snaith and M. Stolterfoht, *Adv. Energy Mater.*, 2021, 2101447.

66 M. Stolterfoht, M. Grischek, P. Caprioglio, C. M. Wolff, E. Gutierrez-Partida, F. Peña-Camargo, D. Rothhardt, S. Zhang, M. Raoufi, J. Wolansky, M. Abdi-Jalebi, S. D. Stranks, S. Albrecht, T. Kirchartz and D. Neher, *Adv. Mater.*, 2020, **32**, 2000080.
67 P. Caprioglio, C. M. Wolff, O. J. Sandberg, A. Armin, B. Rech, S. Albrecht, D. Neher and M. Stolterfoht, *Adv. Energy Mater.*, 2020, **10**, 2000502.
68 A. Onno, C. Chen and Z. C. Holman, in *2019 IEEE 46th Photovoltaic Specialists Conference (PVSC)*, IEEE, 2019, pp. 2329–2333.
69 F. Zu, P. Amsalem, M. Ralaiarisoa, T. Schultz, R. Schlesinger and N. Koch, *ACS Appl. Mater. Interfaces*, 2017, **9**, 41546–41552.
70 D. Shin, F. Zu, A. V. Cohen, Y. Yi, L. Kronik and N. Koch, *Adv. Mater.*, 2021, **33**, 2100211.
71 S. Tao, I. Schmidt, G. Brocks, J. Jiang, I. Tranca, K. Meerholz and S. Olthof, *Nat. Commun.*, 2019, **10**, 2560.
72 M. Burgelman, P. Nollet and S. Degrave, *Thin Solid Films*, 2000, **361–362**, 527–532.

